

# A Novel W-Shaped Flexure-Guided Mechanism for High-Frequency Piezo-Actuated Micromanipulations

Tingting Ye , Student Member, IEEE, Zhao Feng , Member, IEEE, Jie Ling , Member, IEEE, and Yangmin Li , Senior Member, IEEE

**Abstract**—Recently, flexure-guided mechanisms (FGMs) have been increasingly utilized as connectors in high-frequency piezo-actuated micromanipulation systems to suppress off-axis motions. However, out-of-plane motions have been considered less for the design of FGMs, and few efforts have been devoted to the analytical modeling of off-axis motions. This article proposes a novel W-shaped flexure-guided mechanism (WSFGM) with wide bandwidth and compact structure, suppressing both in-plane and out-of-plane off-axis motions. First, the conceptual design of the WSFGM is conducted based on the isosceles triangle theorem. Second, the kinetostatic and dynamic analytical models of off-axis motions of the WSFGM are established based on the modified pseudorigid-body model since its boundary conditions cannot be solved by the traditional counterpart, in which the pseudorigid-body parameters are estimated with the deep neural network to compensate for modeling deviations. After parametric optimization, finite element simulations and experiments are conducted for validation. Results show that the volume of the proposed WSFGM is 5380.2 mm<sup>3</sup>; the axial resonant frequency is tested as 5.951 kHz with a deviation of 5.685%; off-axis resonant frequencies are simulated as all higher than 31 kHz; and average amplitudes of off-axis motions are tested as 12.609 and 10.692 nm under sine signals of 18 kHz.

**Index Terms**—Compliant mechanisms, micromanipulation, piezoelectric actuators (PEAs), pseudorigid-body method (PRBM).

## I. INTRODUCTION

PIEZOELECTRIC actuators (PEAs) show the properties of high precision, wide bandwidth, fast response, and structural compactness [1], [2], [3]. In view of that, piezo-actuated micromanipulation systems with input high-frequency signals have presented numerous advantages over traditional approaches in surgical applications, such as piezo drills in microinjection [4] and ultrasonic scalpels in removing tissue [5], [6]. Such systems are typically composed of a PEA, an end-effector (e.g., microcapillary and scalpel), and a connector between them, as shown in Fig. 1. For example, the PEA can be driven by the high-frequency sinusoidal signal to penetrate oocytes surrounded by high-elastic zona pellucida with microcapillary, in which the survival rate can be remarkably high at approximately 92.5% (versus 77.5% by manual penetration) [7]; the piezoelectric ultrasonic scalpel can be used to remove calcifications in heart valves for faster hemostasis and less damage [8], as shown in Fig. 1(a).

A potential issue with these systems driven by high-frequency signals is that off-axis motions always exist perpendicular to the axis of the end-effector due to unavoidable structural asymmetry, which is also called lateral vibration [9]. The off-axis motion may enlarge the wound of the object, thereby resulting in undesired operational results, such as reducing the cell survival rate [10] or slowing down the tissue healing process [11]. Several studies have been conducted to alleviate this problem by focusing on connectors in piezo-actuated micromanipulation systems. Compared to traditional rigid-body mechanisms, flexure-guided mechanisms (FGMs) have emerged as superior solutions for mitigating off-axis motions. The reason relies on that compliant mechanisms transmit force and displacement through the elastic deformation of flexure segments, leading to strong adaptability due to their compact structure and high precision [12]. For instance, the compliant hinge-based guiding mechanism with parallelogram configuration, as demonstrated in [4], significantly outperformed the traditional rigid connector used in [13] by reducing off-axis displacements of the capillary tip to 0.72  $\mu\text{m}$  impressively, compared to 22  $\mu\text{m}$  in air and 19  $\mu\text{m}$  in water.

To determine the necessary structural geometry and parameters for given target behaviors, conceptual design, approximate modeling, and parametric optimization must be completed

Received 23 May 2024; revised 22 August 2024; accepted 3 October 2024. Recommended by Technical Editor C. Chen and Senior Editor K. Oldham. This work was supported in part by the General Research Fund of Hong Kong under Grant 15206223, in part by the Research Impact Fund of Hong Kong under Grant R5047-22, and in part by the Knowledge Innovation Program of Wuhan-Shuguang Project under Grant 2023010201020252. (Corresponding author: Yangmin Li.)

Tingting Ye and Yangmin Li are with the Department of Industrial and Systems Engineering, The Hong Kong Polytechnic University, Hong Kong 999077, China (e-mail: tilda.ye@connect.polyu.hk; yangmin.li@polyu.edu.hk).

Zhao Feng is with the School of Power and Mechanical Engineering, Wuhan University, Wuhan 430072, China (e-mail: fengzhao@whu.edu.cn).

Jie Ling is with the College of Mechanical & Electrical Engineering, Nanjing University of Aeronautics and Astronautics, Nanjing 210016, China (e-mail: meeijing@nuaa.edu.cn).

Color versions of one or more figures in this article are available at <https://doi.org/10.1109/TMECH.2024.3476332>.

Digital Object Identifier 10.1109/TMECH.2024.3476332

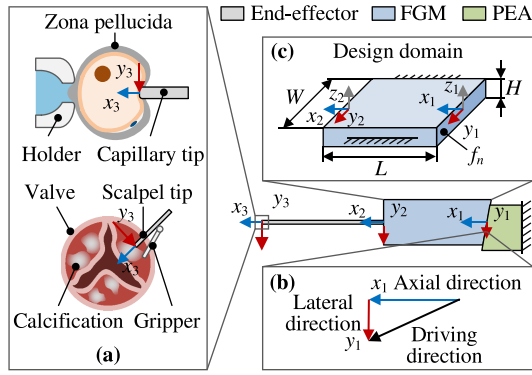


**Fig. 1.** Problem formulation of synthesizing FGM. (a) Potential applications: piezo drill for vibration penetration of oocyte surrounded by zona pellucida, and piezo ultrasonic cutting of calcification of heart valve. (b) Off-axis displacement caused by structural asymmetry. (c) Design domain of FGM.

before physical prototyping [14], [15], [16]. Regarding conceptual design, only the parallelogram configuration based on compliant hinges has been developed for FGMs in piezo-actuated systems with high-frequency signals [7], [17], [18]. On this basis, two same FGMs with parallelogram configuration are assembled orthogonally to realize control of axial ( $x$ -direction) and off-axis ( $y$ -direction) motions [4]. Translational motions in the  $y$ -direction were regarded as minimal optimization objectives in the aforementioned works, while out-of-plane off-axis motions were not considered. There are other linear FGMs of different configurations without consideration of off-axis motions, such as F-shaped configuration [19], Roberts configuration [20], L-shaped configuration [21], etc., whose natural frequencies are too low and their dimensions are too large to be applied to these systems.

To approximate off-axis motions, finite element analysis (FEA) simulations [7], [17] were preferred over mathematical modeling methods. The reason is most likely that off-axis motions belong to irregular directions of motion, which makes it challenging to assume the deformation behaviors and build mathematical formulations. Consequently, it is difficult to gain in-depth insight into how different parameters affect the overall performance, which is not conducive to understanding system behavior and checking whether there are local convergence problems in the optimization process. Besides, most existing FGMs seldom consider their off-axis motions in mathematical modeling. For instance, the pseudorigid-body method (PRBM) is universally employed to conduct the kinetostatic or dynamic modeling of axial motion of linear FGMs [19], [20], [22], which has excellent accuracy and fast speed in small deflection problems of flexure beams. However, it shows limited application for compliant mechanisms with specified boundary conditions, especially for multiple flexure beams sharing the same rotation joint. Moreover, unavoidable deviations are triggered due to overestimated deformations of compliant segments and disregarded deformations of “undeformable” segments. There have been some studies on compensating for modeling errors by estimating nonconstant pseudorigid-body parameters. For example, Jin et al. [23] used polynomial data fitting to obtain the pseudorigid-body parameters by minimizing the difference

between the solutions by PRBM and Bernoulli–Euler beam theory, and Hargrove et al. [24] estimated the counterparts through FEA simulation and experiments.

Overall, the methodological research gaps for generating FGMs in high-frequency piezo-actuated micromanipulations can be summarized as follows.

- 1) Only FGMs with parallelogram configurations have been utilized in high-frequency piezo-actuated micromanipulations to suppress off-axis motions, whereas out-of-plane motions were neglected during design.
- 2) Most FGMs consider off-axis motions less in mathematical modeling.
- 3) Traditional PRBM cannot be applied to some compliant mechanisms with multiple flexure beams sharing the same rotation joint.

To alleviate the aforementioned issues, a novel W-shaped flexure-guided mechanism (WSFGM) with improved performance is proposed for high-frequency piezo-actuated micromanipulations. The contributions of this article can be explained as follows.

- 1) A novel WSFGM with wider bandwidth and smaller size than traditional configurations is proposed, suppressing both in-plane and out-of-plane off-axis motions.
- 2) The analytical modeling and sensitivity analysis of off-axis motions of the proposed WSFGM are performed with the modified pseudorigid-body method (MPRBM).
- 3) MPRBM can be generalized for compliant mechanisms with similar boundary conditions.

The rest of this article is organized as follows. The design objectives, mechanism design, and work principle are stated in Section II. Section III reports the methodology to fulfill the kinetostatic modeling, dynamic modeling, parametric sensitivity, and parametric determination of the proposed WSFGM. Simulation and experimental results are presented for validation and compared to the relevant studies in Section IV. Finally, Section V concludes this article, analyzes the deficiencies, and proposes improvement schemes.

## II. CONCEPTUAL DESIGN

### A. Problem Statement

As shown in Fig. 1(b),  $x$ ,  $y$ , and  $z$  refer to three orthogonal directions of the piezo-actuated system, in which the axial direction is in the  $x$ -direction; subscripts 1–3 refer to positions at the driving end of FGM, the output end of FGM, and the tip of the end-effector, respectively; and  $f_n$  is the  $n$ th-order resonant frequency of FGM. Since the axial inertial force provided by the FGM is positively related to the driving frequency  $f_d$  and axial amplitude  $x_2^{\text{amp}}$ , the resonant frequencies and the off-axis vibration are the main concerns in synthesizing the FGM. On the one hand, it is crucial that the driving frequency  $f_d$  should be far away from the resonant frequencies of the FGM, PEA, and end-effector. Since the natural frequency of PEA is generally several hundred kHz [7], [17], [18], the resonant frequencies of end-effector should be taken seriously. The resonant frequencies of the body of the selected capillary (MPI-0100, Gairdner Tech Company, Ltd) can be simulated as 12.616 and 24.439 kHz via ANSYS, and the counterparts of the tip can be simulated

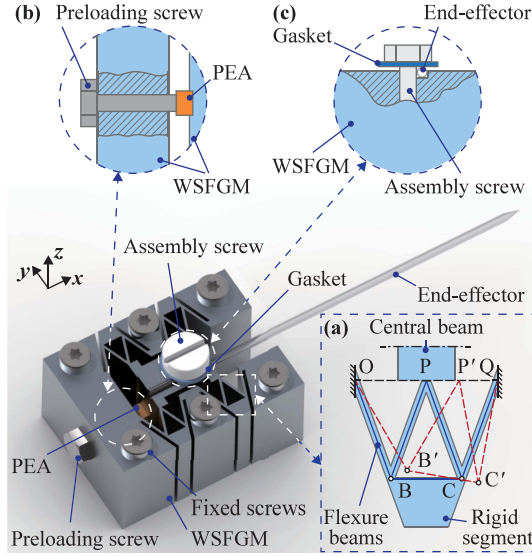


Fig. 2. Design scheme of the micromanipulator for high-frequency piezo-actuated micromanipulations. (a) Diagram and principle of the proposed WSFGM. (b) Mounting and preloading scheme for PEA. (c) Mounting scheme for end-effector.

as 5.290 and 33.078 kHz, in which density is 2260 kg/m<sup>3</sup> and Young's modulus is 63.7 GPa for borosilicate glass. On the other hand, excessive off-axis motions could enlarge wounds, which should be suppressed. In addition, the occupied space must be minimized for better compatibility with micromanipulation.

Therefore, the objective performances of the desired FGM can be determined as follows.

- 1) The resonant frequencies of the FGM  $f_{i-1}$  and  $f_i$  adjacent to the driving frequency  $f_d$  that is determined to be 18 kHz need to be kept away from it, i.e.,  $f_{i-1} \ll f_d \ll f_i$ .
- 2) The amplitudes of off-axis motions need to be reduced to as small as possible.
- 3) The dimension of the design domain of the desired FGM is set to be  $L \times W \times H$  mm<sup>3</sup>, as shown in Fig. 1(c).

### B. Mechanism Design and Work Principle

As shown in Fig. 2, the micromanipulator is composed of an end-effector, a proposed WSFGM, a PEA, a preloading screw, several fixing screws, an assembly screw, and a gasket. The assembly scheme is as follows: the WSFGM is fixed to the base with several fixing screws; the PEA is arranged at the groove of the central beam of the WSFGM to provide the driving force and displacement, which is installed through the preloading screw, as shown in Fig. 2(b); the end-effector is arranged at the groove of the central beam of the WSFGM to serve as the contact end with the manipulation object, which is installed with the assembly screw and the gasket, as shown in Fig. 2(c).

The WSFGM needs to be proposed for a connector between the end-effector and the PEA, which can effectively suppress the off-axis vibrations. The core parts of the proposed WSFGM are four identical compliant elements, symmetrically distributed on both sides of the central beam. Inspired by the traditional Roberts mechanism, one of the compliant elements is depicted,

comprising four flexure beams and one rigid segment, as shown in Fig. 2(a). The geometric relationship of the proposed WSFGM is as follows:

$$\overline{OB} = \overline{BP} = \overline{CP} = \overline{CQ} \quad (1)$$

where points O and Q are fixed. Due to the constraints of the isosceles triangles, it can be seen that point P strictly keeps moving on the straight line OQ.

## III. MODELING AND PARAMETRIC DETERMINATION

### A. Kinetostatic Modeling

Since the traditional PRBM is not applicable to the proposed WSFGM due to its boundary conditions, tension and compression deformations that should not be there occur in axial motions, leading to impractical motions. Therefore, MPRBM is proposed to approximate the axial and off-axis motions. As shown in Fig. 3(a), the proposed WSFGM is composed of four identical compliant elements, symmetrically distributed on both sides of the central beam. As for one element, each flexure beam is equivalent to a pseudorigid-body mechanism, which is composed of a rigid rod that cannot be deformed axially, a torsion spring rotating hinge at both ends of this rod, and a linear spring that can only be deformed axially. Assuming that the virtual driving force/torque is applied to the input end of WSFGM, the reaction force/torque at the output end of WSFGM can be represented as  $\delta D_2 = [F_X, F_Y, F_Z, F_\theta, F_\psi]^T$ , where  $\theta$  and  $\psi$  refer to the directions of rotation around axes  $y$  and  $z$ . The driving torque around axis  $x$  is hardly produced by PEA, and therefore ignored.

The motion of the WSFGM is orthogonally decomposed into five degrees of freedom (DOFs), as shown in Fig. 3(b)–(i). Taking the driving force  $F_X$  as an example, the pseudorigid-body model of one compliant element under  $F_X$  can be established in Fig. 3(b), in which  $\delta X$  refers to the virtual displacement caused by  $F_X$ . There are  $M$  ( $M = 6$ ) pseudotororsion springs, including  $A_i B_i$ ,  $B_i C_i$ ,  $D_i E_i$ , and  $F_i$ , in which  $k_{rx}$  refers to their rotation stiffness. There are  $N$  ( $N = 4$ ) pseudolinear springs, including  $O_i A_i$ ,  $P_i E_i$ ,  $P_i F_i$ , and  $Q_i D_i$ , in which  $k_{t1}$  and  $k_{t2}$  refer to linear stiffness of outer and inner counterparts. Since there are four identical compliant elements,  $4M$  pseudotororsion springs and  $4N$  pseudolinear springs are presented for the whole WSFGM. Besides, the mass of pseudorigid rods  $A_i B_i$ ,  $B_i C_i$ ,  $C_i E_i$ , and  $C_i D_i$  is concentrated at the particles as  $m_B$ ;  $m_R$  and  $m_C$  are the concentrated mass of pseudorigid rods  $B_i C_i$  and central beam, respectively. The pseudorigid-body models of one compliant element under  $F_Y$  and  $F_Z$  can also be established similarly, as shown in Fig. 3(c) and (d), respectively. As for the driving torque  $F_\theta$ , the pseudorigid-body model of the central beam in  $\theta$  direction can be established in Fig. 3(e), in which  $\delta \Theta$  refers to the virtual displacement caused by  $F_\theta$ . The orthogonal displacement components in  $x$  and  $z$  directions of  $\delta \Theta$  are  $\delta \theta_X$  and  $\delta \theta_Z$ , as shown in Fig. 3(h) and (g), respectively. The pseudorigid-body model of the central beam in  $\psi$  direction can also be established in Fig. 3(f) similarly, whose orthogonal displacement components in  $x$  and  $y$  directions are  $\delta \Psi_X$  and  $\delta \Psi_Y$ , as shown in Fig. 3(h) and (i), respectively.



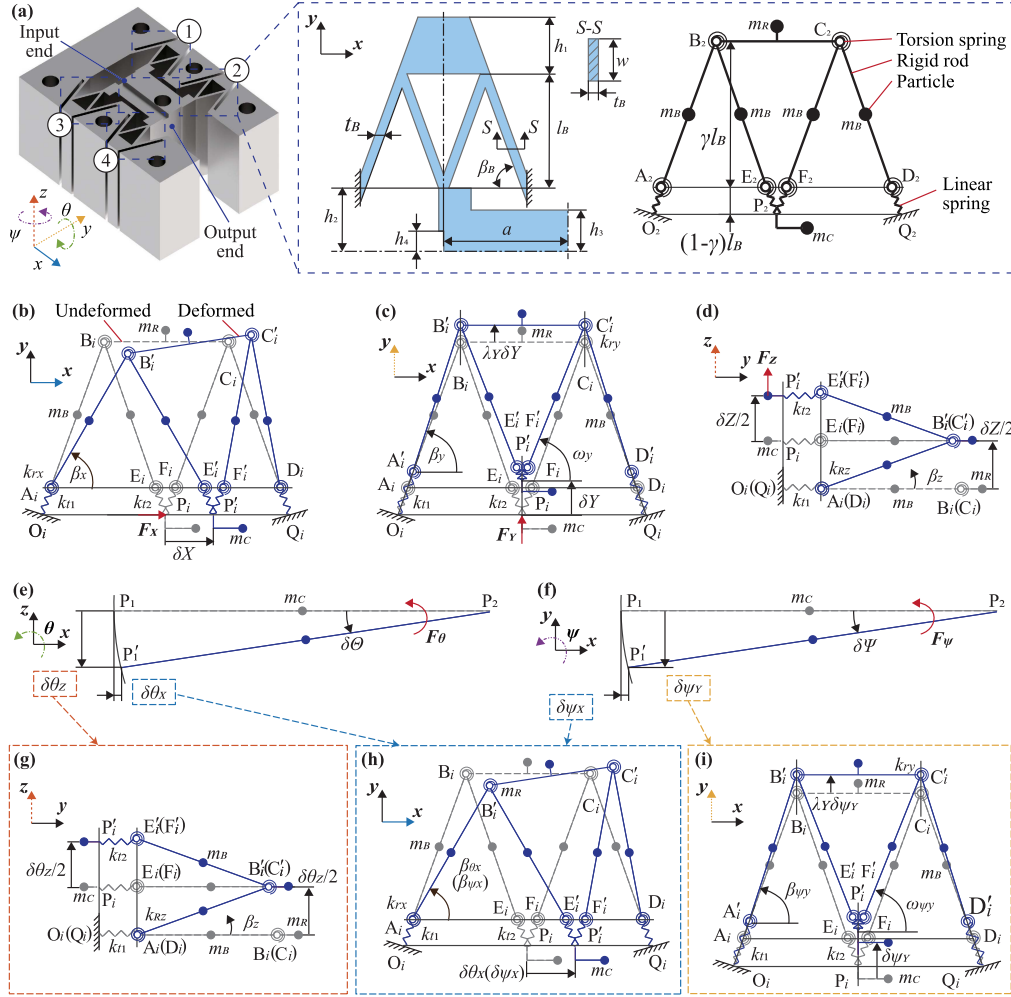


Fig. 3. Analytical modeling of the proposed WSFGM. (a) Illustration of pseudorigid-body transformation. (b) Model of one element in the  $x$ -direction. (c) Model of one element in the  $y$ -direction. (d) Model of one element in the  $z$ -direction. (e) Model of central beam in the  $\theta$  direction. (f) Model of central beam in the  $\psi$  direction. (g)–(i) Orthogonal displacement components of virtual rotation displacements  $\delta\Theta$  and  $\delta\Psi$ .

According to the principle of virtual work, the static governing equation can be established as

$$\delta W_d + \sum_i^{4(M+N)} \delta W_{si} = 0 \quad (2)$$

where  $\delta W_d$  refers to the virtual work done by the driving force, and  $\delta W_{si}$  refers to the virtual work done by the resisting force/moment on the  $i$ th pseudo spring, in which  $i = 1, 2, \dots, 4(M+N)$ .

Based on (2), it can be obtained that

$$\frac{1}{2} k_j q_j^2 = \frac{1}{2} \sum_i^{4(M+N)} k_{si} q_{si}^2 \quad (3)$$

where  $k_j$  and  $q_j$  refer to equivalent stiffness and virtual displacement of WSFGM in the  $j$ th DOF, respectively, in which  $j = x, y, z, \theta, \psi$ ; and  $k_{si}$  and  $q_{si}$  refer to equivalent stiffness and virtual displacement of the  $i$ th pseudo spring, respectively, in which the value of displacement of torsion spring refers to its

rotation angle, and the counterpart of linear spring refers to its change of length.

According to the geometric relationship, the unit vectors of virtual displacements of pseudosprings in five DOFs can form a matrix  $U_s^* \in \mathbb{R}^{5 \times 7}$

$$U_s^* = \begin{bmatrix} R_s^* & T_s^* \end{bmatrix} \quad (4)$$

where  $R_s^*$  and  $T_s^*$  refer to angular (right-hand rule) and linear displacements of torsion springs and linear springs

$$R_s^* = \begin{bmatrix} \alpha_x & 0 & 0 & 0 & 0 \\ 0 & \alpha_y & 0 & 0 & 0 \\ 0 & 0 & \alpha_z & 0 & 0 \\ \alpha_{\theta x} & 0 & -\alpha_{\theta z} & \alpha_{\theta} & 0 \\ \alpha_{\psi x} & -\alpha_{\psi y} & 0 & 0 & \alpha_{\psi} \end{bmatrix}$$

$$T_s^* = \begin{bmatrix} 0 & \sqrt{2}g(\alpha_y) & 0 & 0 & g(\alpha_{\psi y}) \\ 0 & \sqrt{2}g(-\alpha_y) & 0 & 0 & g(-\alpha_{\psi y}) \end{bmatrix}^T \quad (5)$$

where  $\alpha_j$  refers to change of  $\beta_j$ ,  $\alpha_{\theta j}$  refers to change of  $\beta_{\theta j}$  caused by displacement  $\delta\theta_j$ , as does  $\alpha_{\psi j}$ , and  $g(x)$  is defined as

$$g(x) = \frac{\gamma l_B}{\sqrt{2} \sin \beta_B} \left[ 1 - \frac{\cos(\beta_B + x)}{\cos \beta_B} \right]. \quad (6)$$

Then, the dimensionless quantity of counterparts can be represented as a matrix  $Q_s \in \mathbb{R}^{7 \times 10}$

$$Q_s = \begin{bmatrix} R_s & T_s \end{bmatrix} \quad (7)$$

where

$$R_s = \begin{bmatrix} 2 & -2 & -2 & 2 & -2 & -2 \\ 2 & 4 & -4 & -2 & 2 & -2 \\ 2 & 0 & 0 & 2 & -2 & -2 \\ 0 & 1 & 1 & 0 & 1 & 1 \\ 0 & 0 & 0 & 0 & 2 & 2 \end{bmatrix}, T_s = \begin{bmatrix} 2 & 0 \\ 0 & 2 \\ 0 & 2 \\ 2 & 0 \end{bmatrix}^T. \quad (8)$$

Note that, by considering force equilibrium and energy conservation, the displacement component ratio  $\lambda_Y$  can be derived as 1/2, as shown in Fig. 3(c).

Then, the stiffness matrix  $K_s$  of pseudosprings can be determined as

$$K_s = \begin{bmatrix} K_R & \\ & K_T \end{bmatrix} \quad (9)$$

where  $K_R$  represents the  $5 \times 5$  diagonal matrix of equivalent stiffness for torsion springs, as  $\text{diag}(k_{rj})$ , and  $K_T$  represents the  $2 \times 2$  diagonal matrix of equivalent stiffness for linear springs, as  $\text{diag}(k_{tj})$ .

Combining (4)–(9), the virtual work matrix  $W_s$  of pseudosprings can be derived as

$$W_s = -\frac{1}{2} U_s^{*[2]} K_s Q_s^{[2]} \quad (10)$$

where  $A^{[2]} = A \circ A$ , in which  $\circ$  refers to the Hadamard product.

Substituting (10) into (3), the equivalent stiffness  $k_j$  of WS-FGM in each DOF can be achieved as

$$k_j = 2 \| -W_{sj} \|_1 / q_j^2 \quad (11)$$

where  $\|W_{sj}\|_1$  refers to the 1-norm of the  $j$ th row vector of  $W_s$ .

## B. Dynamic Modeling

According to Lagrange's equation, the dynamic governing equation can be established as

$$m_j \ddot{q}_j(t) + c_j \dot{q}_j(t) + k_j q_j(t) = P_j(t) \quad (12)$$

where  $m_j$ ,  $c_j$ , and  $P_j(t)$  refer to the equivalent mass, damping coefficient, and driving force in the  $j$ th DOF, respectively.

Using the energy method,  $m_j$  can be obtained as

$$m_j = \sum_k m_{rk} \left( \frac{dq_{rk}}{dq_j} \right)^2 \quad (13)$$

where  $m_{rk}$  and  $q_{rk}$  refer to equivalent mass and virtual displacement of the  $k$ th pseudorigid rod.

On this basis, the unit vectors of virtual displacement gradients of pseudorigid rods concerning  $q_j$  can be represented as

$$\nabla U_r^* = \begin{bmatrix} \nabla R_r^* & \nabla T_r^* \end{bmatrix} \quad (14)$$

where  $\nabla R_r^*$  and  $\nabla T_r^*$  refer to angular and linear counterparts

$$\nabla R_r^* = \nabla R_s^* \\ \nabla T_r^* = \begin{bmatrix} 1 & 0 & 0 & 0 & 0 \\ 0 & 1 & 0 & 0 & -2a \cos \alpha_\psi \\ 0 & 0 & 1 & -2a \cos \alpha_\theta & 0 \end{bmatrix}^T. \quad (15)$$

Then, the equivalent mass of WSFGM in each DOF can be achieved as

$$m_j = \|M_{ej}\|_1 \quad (16)$$

where  $M_{ej}$  is the  $j$ th row vector of  $M_e$

$$M_e = \nabla U_r^{*[2]} M_r \quad (17)$$

where  $M_r \in \mathbb{R}^{8 \times 12}$

$$M_r = \begin{bmatrix} J_R & \\ & M_T \end{bmatrix} \\ J_R = \begin{bmatrix} 4J_{B1} & 4J_{B1} & 4J_{B1} & 4J_{B1} & 4J_{R1} & 0 \\ 4J_{B1} & 4J_{B1} & 4J_{B1} & 4J_{B1} & 4J_{R1} & 0 \\ 4J_{B2} & 4J_{B2} & 4J_{B2} & 4J_{B2} & 4J_{R2} & 0 \\ J_{B3} & J_{B3} & J_{B3} & J_{B3} & J_{R3} & J_C \\ 0 & 0 & 0 & 0 & 0 & J_C \end{bmatrix} \\ M_T = \begin{bmatrix} 0 & 0 & 0 & 0 & 0 & m_C \\ m_B & m_B & m_B & m_B & m_R & m_C \\ 0 & 0 & 0 & 0 & 0 & m_C \end{bmatrix} \quad (18)$$

where  $J_{ji}$  is the moment of inertia of the  $i$ th pseudorigid rod in the  $j$ th DOF.

Let  $p_j = 0$  and  $c_j = 0$ , and the resonant frequencies  $f_j$  can be calculated as

$$f_j = \frac{1}{2\pi} \sqrt{\frac{k_j}{m_j}}. \quad (19)$$

To facilitate the characterization of the off-axis vibration suppression effect of the proposed WSFGM,  $R_{VS}$  is defined as the ratio of the off-axis displacements at the output end to the input end according to the mode superposition method

$$R_{VS} = \sqrt{\frac{R_{dy}^2 + R_{dz}^2}{\left(1 + 4a^2 R_{d\psi} \frac{k_y}{k_\psi}\right)^2 + \left(1 + 4a^2 R_{d\theta} \frac{k_z}{k_\theta}\right)^2}} \quad (20)$$

where static displacements in  $y$  and  $z$  directions are assumed to be the same, and the dynamic magnification ratio is obtained as

$$R_{dj} = |1 - f_d^2 / f_j^2|^{-1}. \quad (21)$$

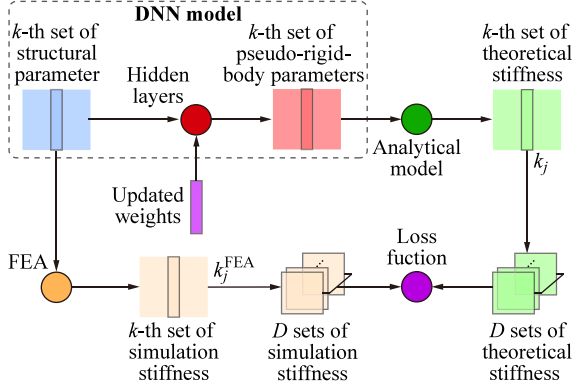


Fig. 4. Illustration of the DNN model.

### C. Estimation of Pseudorigid-Body Parameters

With references to [12] and [25], the bending, torsional, and tension–compression stiffness of flexure beams can be equivalent to

$$\begin{aligned} k_{rx} &= k_{ry} = k_{rz} = 2C_m \gamma \kappa_{rj} E I_{rj} \sin \beta_B / l_B \\ k_{rz} &= 2C_m \gamma \kappa_{rz} E I_{rz} \sin^4 \beta_B / l_B \\ k_{r\theta} &= C_m \gamma \kappa_{r\theta} E I_{r\theta} \sin \beta_B / [2(1 + \mu) l_B] \\ k_{t1} &= k_{t2} = C_m \kappa_t E A_t \sin \beta_B / l_B \end{aligned} \quad (22)$$

where  $E$  and  $\mu$  refer to Young's modulus and Poisson's ratio of the selected material of WSFGM, which are given in Section IV-B;  $E/(2 + 2\mu)$  refers to shear modulus;  $\gamma$  refers to the characteristic radius factor ( $0 < \gamma < 1$ );  $\kappa_{rj}$  and  $\kappa_t$  refer to the normalized stiffness coefficients ( $0 < \kappa_{rj}, \kappa_t < 1$ ), in which  $j = x, y, z, \theta, \psi$ , and the maximum value is set to be  $C_m$  as 3; and  $I_{rj}$  and  $A_t$  refer to the moment of inertia and the sectional area of flexure beams, respectively.

However, the rigid segments are regarded as undeformable, which causes the virtual work done by the compliant segments in (10) to be overestimated theoretically, while the virtual work done by the rigid segments is ignored, leading to unavoidable modeling deviation. To compensate for the modeling deviations, the deep neural network (DNN) model is involved in estimating the pseudorigid-body parameters, containing the characteristic radius factor  $\gamma$  and the stiffness coefficients  $\kappa_{rj}$  and  $\kappa_t$ .

The DNN model is given in Fig. 4. Specifically,  $10^5$  sets of structural parameters are selected randomly for FEA simulations to establish the dataset, in which training and testing sets are independent and as 7:3. The selected ranges of structural parameters are determined according to geometric constraints and prior experience, as given in Table I. Using an FEA simulation as an example, the equivalent stiffness of WSFGM is obtained by applying the driving force to the input end and the displacement at the output end. Several iterations are conducted via ANSYS APDL to construct the whole dataset.

The DNN model is established with one input layer, two hidden layers, and one output layer. The input layer contains nine neurons that represent the structural parameters, including  $l_B, t_B, \beta_B, h_1, h_2, h_3, h_4, a$ , and  $w$ ; two hidden layers both

TABLE I  
RANGES AND OPTIMIZED VALUES OF STRUCTURAL PARAMETERS

| Item          | Range        | Value | Item       | Range    | Value |
|---------------|--------------|-------|------------|----------|-------|
| $l_B$ (mm)    | [2.5, 5.5]   | 3.76  | $h_1$ (mm) | [1.8, 4] | 1.88  |
| $t_B$ (mm)    | [0.15, 0.35] | 0.32  | $h_2$ (mm) | [3.5, 8] | 3.50  |
| $\beta_B$ (°) | [45, 80]     | 70.1  | $h_3$ (mm) | [2.5, 3] | 2.50  |
| $a$ (mm)      | [3, 12]      | 3.99  | $h_4$ (mm) | /        | 1.50  |
| $w$ (mm)      | [4, 12]      | 12    |            |          |       |

TABLE II  
FORMULATION OF CONSTRAINT OPTIMIZATION

|   |  |  |  |  |  |
|---|--|--|--|--|--|
| <i>Objectives:</i> min: $\sigma_1 = \max\{1/ f_d - f_j \}$ , $\sigma_2 = R_{VS}$ , $\sigma_3 = LWH$   |  |  |  |  |  |
| <i>Variables:</i> $\{p\} = \{l_B, t_B, \beta_B, h_1, h_2, h_3, h_4, a, w\}$   |  |  |  |  |  |
| <i>Constraints:</i>   |  |  |  |  |  |
| (i) According to geometric constraints, it gives that $p_i > 0$ , $a \geq 2l_B \cot \beta_B + t_B + 1.2$ , $h_2 - h_3 > t_B \tan \beta_B / 2 + 0.5$ , and $h_2 > h_3 > h_4$ .               |  |  |  |  |  |
| (ii) To reduce the deformation of the pseudo-rigid segments, it gives that $12 \geq w \geq 4$ , $6 \geq h_1 \geq 1.5$ , and $10 \geq h_3 \geq 2.5$ .  |  |  |  |  |  |
| (iii) Considering flexure and assembly requirements, it gives that $1.2 \geq t_B \sin \beta_B \geq 0.3$ , $10 \geq l_B / \sin \beta_B \geq 4$ , and $80^\circ \geq \beta_B \geq 45^\circ$ . |  |  |  |  |  |
| (iv) Regarding dimensional miniaturization, it gives that $750 \geq LW = 4(a + l_B \tan \beta_B)(h_1 + l_B + h_2)$ .  |  |  |  |  |  |

contain 256 neurons; *Tanh* function is employed as the nonlinear activation function; the output layer contains seven neurons that represent the normalized pseudorigid-body parameters, including  $\gamma, \kappa_{rx}, \kappa_{ry}, \kappa_{rz}, \kappa_{r\theta}$ , and  $\kappa_{r\psi}$ ; the backpropagation algorithm is used to solve the gradient; and the loss function is determined as

$$e = \frac{1}{D} \sum \sum_j |(k_j - k_j^{\text{FEA}}) / k_j^{\text{FEA}}| \quad (23)$$

where  $k_j$  refers to the theoretical stiffness in the  $j$ th DOF in (11),  $k_j^{\text{FEA}}$  refers to the simulation stiffness in the  $j$ th DOF,  $D$  refers to sets of training or testing samples, and the Adam algorithm [26] is adopted as the gradient descent optimizer.

The training sets, including structural parameters, each theoretical stiffness  $k_j$ , and corresponding simulation stiffness  $k_j^{\text{FEA}}$  are imported into the DNN model, in which the iteration and epoch are set to be 70 and 20. To validate the effectiveness of the DNN model in the whole design domain, the testing sets are imported into the trained DNN model. After that, the trained DNN model can be utilized to calculate the stiffness matrix in (9) with given structural parameters.

### D. Sensitivity and Determination of Structural Parameters

Based on the genetic algorithm, the *gamultiobj* function in MATLAB is used to perform multiobjective parameter optimization of the structural parameters of the proposed WSFGM. The constraint optimization of structural parameters is formulated in Table II. The minimizing objective function is defined concerning wider high-frequency bandwidth  $\sigma_1$ , smaller off-axis motions  $\sigma_2$ , and miniaturized dimension  $\sigma_3$ . The variables are

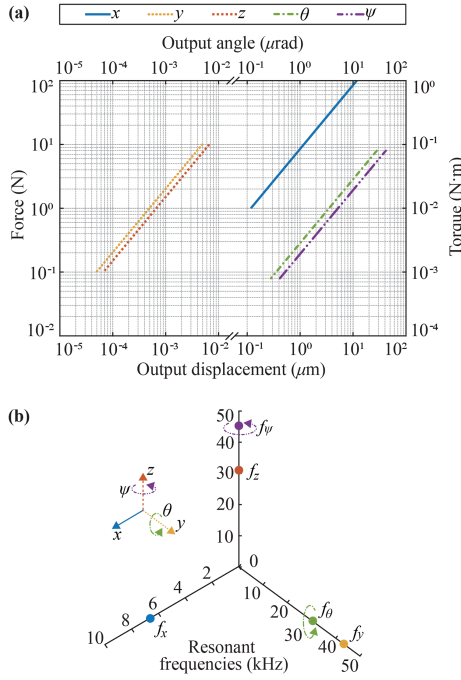


Fig. 5. Analytical results. (a) Equivalent stiffness. (b) Resonant frequencies.

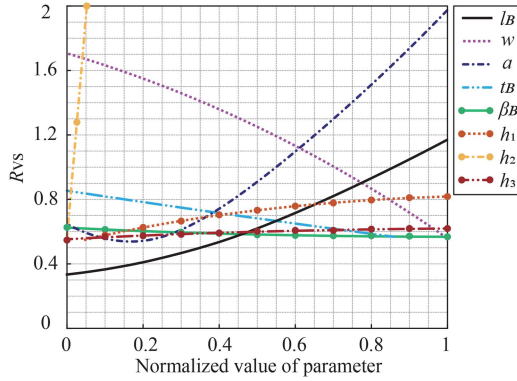


Fig. 6. Parametric sensitivity of off-axis vibration suppression ratio  $R_{VS}$ .

composed of nine structural parameters. To reduce the deformation of the pseudorigid segments with consideration of manufacturing limitations, assembly requirements, and structural limitations, the constraint functions are defined.

With specified ranges of parameters in Table I, the Pareto front solutions can be obtained. The solution with the smallest  $\sigma_2$  is given priority. The optimized values of structural parameters are given in Table I. As shown in Fig. 5, analytical results show that the equivalent stiffness is almost constant during working stroke; the resonant frequencies are calculated as 6.317, 31.282, 31.832, 42.935, and 45.106 kHz, whose corresponding mode shapes are distributed in  $x$ ,  $\theta$ ,  $z$ ,  $y$ , and  $\psi$  directions, respectively; and  $R_{VS}$  is obtained as 0.570 referring to (20).

As shown in Fig. 6, the parametric sensitivity of off-axis vibration suppression ratio  $R_{VS}$  under driving signals of 18 kHz with main structural parameters is analyzed. For each structural

parameter, the available trials under the geometric limitations are conducted, in which others take unified values. The ranges of the structural parameters are taken from Table I. The results show that parameters  $\beta_B$  and  $h_3$  have little impacts on  $R_{VS}$ ; parameters  $t_B$  and  $h_1$  have small impacts; parameters  $l_B$ ,  $w$ , and  $a$  have relatively higher impacts; and parameter  $h_2$  has significantly high impacts. Besides, all other parameters change monotonically within the selection range, except for parameter  $a$ . Browsing the lowest point of  $R_{VS}$  of each curve, it can be observed that they are consistent with the optimized parameters in Table I, indicating that the parameter optimization is not confronted with local convergence. Particularly, parameter  $h_4$  is disregarded due to the limited ranges specified by the assembly requirement of PEA.

## IV. VALIDATION

### A. Simulation Validation

To validate the effectiveness of analytical modeling, FEA simulations are conducted via ANSYS, including modal, harmonic response, and transient response analyses. Since the WSFGM works in the air, the damping ratio is not considered in FEA simulations of the WSFGM.

As shown in Fig. 7(a), the fixed constraints are set at the fixed holes of WSFGM, in which the element size of the flexure beams is refined to 0.15 mm. According to the modal analysis, the first six resonant frequencies can be obtained as 6.289, 31.161, 31.996, 42.816, 43.786, and 45.260 kHz, whose corresponding mode shapes are mainly distributed in  $x$ ,  $\theta$ ,  $z$ ,  $y$ ,  $\varphi$ , and  $\psi$  directions, respectively. Therefore, the validity of the analytical modeling of resonant frequencies can be verified.

As shown in Fig. 7(b), the harmonic response analysis is conducted, in which the input force in the  $x$ -direction is ten times the counterparts in the  $y$  and  $z$  directions. Around 6.3 kHz, the harmonic response at the output end of WSFGM demonstrates its greatest prominence in the  $x$ -direction, while relatively imperceptible in other directions. The remaining steady amplitudes across other resonant frequencies can also support the result of the modal analysis.

As shown in Fig. 7(c), the transient response analysis is conducted with input sinusoidal amplitudes of  $x_1$  as 0.5 μm,  $y_1$  as 0.05 μm, and  $z_1$  as 0.05 μm. The driving frequency is set as 18 kHz. Results show that the maximum stress that occurs in flexure beams is 1.374 MPa; the maximum output amplitudes in off-axis directions of  $y_2$ ,  $z_2$ ,  $\theta_2$ , and  $\psi_2$  are 0.013 μm, 0.039 μm, 1.681 μrad, and 4.832 μrad, respectively. Then, the off-axis vibration suppression ratio can be derived as 0.581.

In addition, transient simulations are conducted to evaluate the attenuation of PEA performances by the proposed WSFGM. Concerning damping effects and mechanical losses, the deformation of the proposed WSFGM brings losses in driving energy provided by PEA. The maximum output amplitude in axial direction  $x_2$  is 0.522 μm with the same input sinusoidal signal, as shown in Fig. 7(c), larger than the input amplitude. The reason is probably that the central beam suffered tension and compression deformation during this process. Neither frequency nor phase changes. It can be inferred that there is no reduction



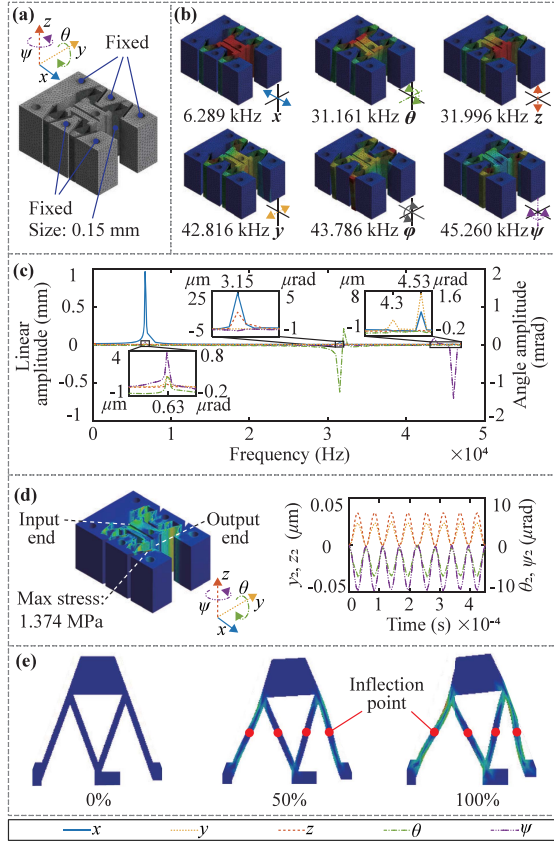


Fig. 7. Simulation results. (a) Finite element model. (b) Modal simulation result. (c) Harmonic response simulation result. (d) Transient response simulation result: stress distribution and output off-axis displacements. (e) Deformed shapes of flexure beams under 0%, 50%, and 100% amplitude of inputs.

in displacement, slower response time, and attenuation of frequency caused by WSFGM. Moreover, the buckling of flexure beams may reduce system stability, degrading the precision and responsiveness of PEA. Hence, the deformed shapes of flexure beams in the proposed WSFGM under 0%, 50%, and 100% amplitude of input displacements are presented, as shown in Fig. 7(e). Through the whole stroke, only one inflection point exists in each flexure beam, indicating no buckling situation.

### B. Experimental Validation

The physical prototype of the proposed WSFGM is fabricated by slow wire electrical discharge machining with 65 Mn spring steel, whose density  $\rho$  is 7850 kg/m<sup>3</sup>, Young's modulus  $E$  is 200 GPa, Poisson's ratio  $\mu$  is 0.3, and Yield strength is 784 MPa. The dimension of the physical prototype is measured as  $24.5 \times 18.3 \times 12$  (5380.2) mm<sup>3</sup>. The experimental system setup is shown in Fig. 8(a). The blue arrow refers to the control signal, and the red arrow refers to the sensor signal. As for the transmission of sensor signals, the output analog signals of the WSFGM are collected by laser sensors (model: Keyence LK-H025). Then, the output analog signals are transmitted to the 12-bit analog-to-digital converter (model: NI-9201, analog input voltage range:  $-10$  to  $10$  V), which is installed on the

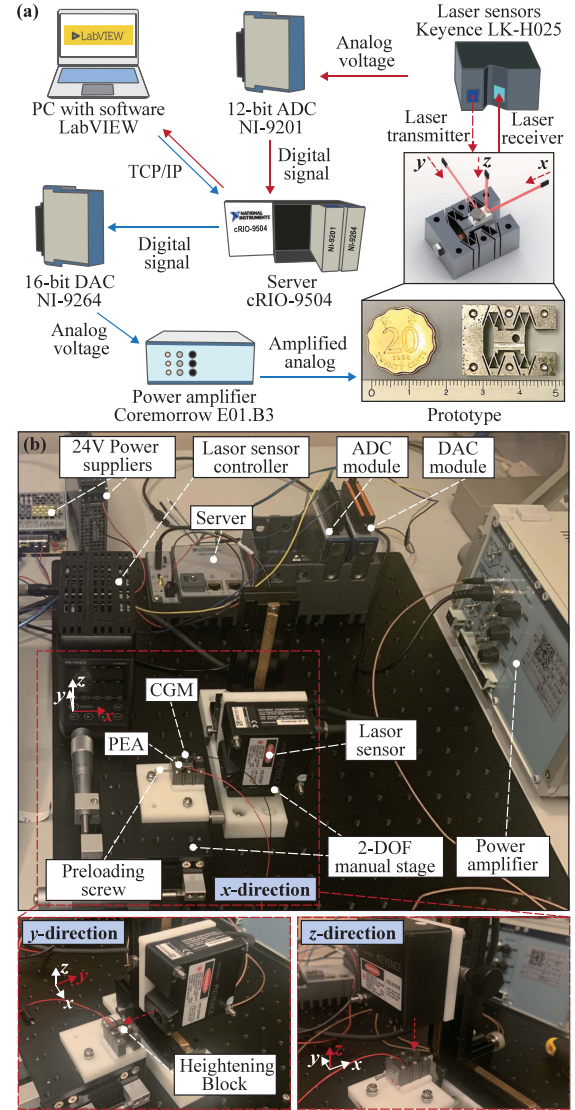


Fig. 8. Experimental system setup. (a) Rapid prototyping control system. (b) Physical experimental platform with three layouts.

server (model: NI cRIO-9504). At last, the personal computer (PC) with the software LabVIEW receives and displays the digital signals. As for the transmission of control signals, the input digital signals are sent from the PC with the software LabVIEW. Then, the input digital signals are transmitted to the 16-bit digital-to-analog converter (model: NI-9264, analog output voltage range:  $-10$  to  $10$  V), which is installed on the server. Through the power amplifier (model: Aigtek ATAP2010, bandwidth:  $\sim 20$  kHz, maximum output power: 1300 Wp, output voltage:  $-20$  to  $130$  V, maximum output current: 10 Ap), the analog signals are amplified and transmitted to the PEA (model: Coremorrow NAC2001, maximum driving voltage: 60 V, stroke: 3  $\mu\text{m}$ , resonant frequency: 486 kHz, electrostatic capacitance: 150 nF, thrust: 168 N) of the prototype of WSFGM. The average driving power of PEA can be calculated as 8.1–10.8 W of sine wave signal under 15–20 kHz, indicating that the power amplifier can meet the requirements. As shown in Fig. 8(b), an XY manual stage and an X(Y)Z manual stage are utilized for



TABLE III  
COMPARISON OF PHYSICAL PROPERTIES OF RELATED FGMS

| Reference                                | [7]           | [17]          | [19]      | [20]    | [21]       | This work                   |
|--|---------------|---------------|-----------|---------|------------|-----------------------------|
| Configuration                            | Parallelogram | Parallelogram | F-shaped  | Roberts | L-shaped   | W-shaped                    |
| Modeling method                          | FEA           | FEA           | PRBM      | PRBM    | PRBM       | MPRBM                       |
| Analytical modeling of off-axis motions  | ×             | ×             | ×         | ×       | ×          | ✓                           |
| Suppression of off-axis motions          | $y$           | $y$           | /         | /       | /          | $y, z, \psi$ , and $\theta$ |
| $L \times W \times H$ (mm <sup>3</sup> ) | 37×43 ×5      | 37×43×5       | 100×64×10 | 20×60×4 | 240×240×12 | 24.5×18.3×12                |
| Axial resonant frequency (Hz)            | 1650          | 24 927        | 856.9     | 1006    | 90.5       | 6289.4                      |
| Lowest off-axis resonant frequency (Hz)  | 2180          | 27 151        | /         | /       | /          | 31 161                      |

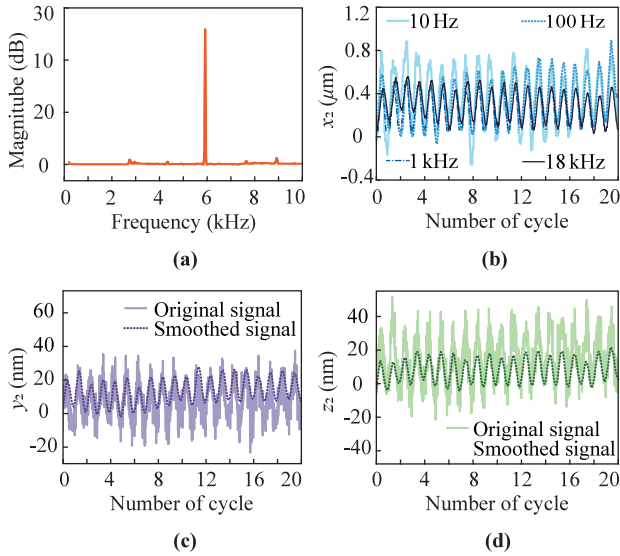


Fig. 9. Experimental results. (a) Power spectrum from 10 Hz to 10 kHz. (b) Output displacement in the  $x$ -direction at output end. (c) Output displacement in the  $y$ -direction at output end. (d) Output displacement in the  $z$ -direction at output end.

the alignment of the prototype of WSFGM and the laser sensor. Three layouts are arranged to measure the output displacements of the prototype of WSFGM in  $x$ ,  $y$ , and  $z$  directions, respectively. Especially, a heightening block fabricated by 3-D printing is assembled above the prototype of WSFGM, since the output displacement of WSFGM in the  $y$ -direction cannot be measured directly due to geometric restrictions.

As shown in Fig. 9(a), the first-order resonant frequency of the prototype is tested as 5.951 kHz with the swept sine signal from 10 Hz to 10 kHz, in which the modeling and simulation deviations are 5.685% and 6.150%. The deviations might be caused by the modeling simplification, manufacturing defects, and material inhomogeneities. However, subsequent wave peaks cannot be observed due to the influence of high-frequency noise and the limitations of the power amplifier. The sine signals within the duration of 20 cycles from 10 Hz to 18 kHz are provided. Given the voltage amplitude of 1.5 V, the average drive amplitude is tested as  $0.390 \mu\text{m}$  at 10 Hz by measuring the input displacements. As shown in Fig. 9(b), the average amplitudes of output displacement in the  $x$ -direction at the output end  $x_2$  are tested as  $0.390 \pm 0.119$ ,  $0.313 \pm 0.096$ ,  $0.251 \pm 0.031$ , and  $0.213 \pm 0.024 \mu\text{m}$  at 10 Hz, 100 Hz, 1 kHz, and 18 kHz, respectively.

It can be seen that the curve in the low-frequency range has slow drift and large fluctuation, which may be caused by the laser drift of displacement sensors. Meanwhile, the possibility of this conjecture has been improved, since the fluctuation problem in the high-frequency area has been significantly improved. On this basis, the experiments in  $y$  and  $z$  directions at low-frequency range are hard to be conducted, since their displacements are much smaller than the fluctuations. As shown in Fig. 9(c) and (d), the output displacements in  $y$  and  $z$  directions at the output end  $y_2$  and  $z_2$  under the driving frequency of 18 kHz are tested and smoothed. Results show that the average amplitudes of smoothed curves are calculated as  $12.609 \pm 1.527$  and  $10.692 \pm 1.329 \text{ nm}$ .

### C. Discussions

The physical properties of existing FGMS are summarized in Table III, in which the configuration, modeling method, volume, and resonant frequencies are taken into account. Compared to related works, the proposed WSFGM is relatively miniaturized, which means excellent compatibility with micromanipulation; suppression of both in-plane ( $y$ -direction) and out-of-plane motions were considered during design process; the lowest off-axis resonant frequencies of those FGMS can illustrate that the attainable frequency of the proposed WSFGM is relatively higher and the available bandwidth is wider; and the analytical modeling of off-axis motions of WSFGM is established by the proposed MPRBM.

However, there is still something that can be improved in this work. First, the vibration of WSFGM in the  $y$ -direction could not be measured directly due to geometric restrictions, in which inaccuracies were introduced in the measured displacement. Second, MPRBM is established with 1R, which can meet the requirement for the proposed WSFGM, lacking compatibility of compliant mechanisms with large deformation.

### V. CONCLUSION

The main works in this article are summarized as follows. First, the conceptual design of the WSFGM was conducted based on the isosceles triangle theorem. Second, the kinetostatic and dynamic analytical models of off-axis vibrations of the proposed WSFGM were proposed based on the MPRBM, in which the DNN model based on FEA simulations was designed to compensate for modeling errors. Then, the structural parameters were determined with constrained multiobjective optimization using the genetic algorithm. Next, the FEA simulations and

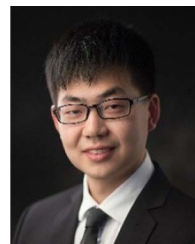
experiments were conducted for validation. The results show that the volume of the proposed WSFGM is about  $5380.2 \text{ mm}^3$ ; the first six resonant frequencies are 6.289, 31.161, 31.996, 42.816, 43.786, and 45.260 kHz; and the off-axis vibration suppression ratio can be derived as 0.570. Finally, the physical prototype was manufactured through slow wire electrical discharge machining to conduct the experiments. Experimental results show that the first-order resonant frequency is tested as 5.951 kHz; the deviations of first-order resonant frequencies through modeling and simulation with experimental results are 5.685% and 6.150%; and average amplitudes of off-axis motions are tested as 12.609 and 10.692 nm under sine signals of 18 kHz. In the future, 2R or 3R PRBM will be considered for compliant mechanisms with large deformation to increase generalizability; alternative analytical modeling methods, such as the elliptical integration method and the chain beam constraint method, will be explored to replace FEA simulation for dataset generation; and introducing algorithms such as the attention mechanism could help streamline the neural network architecture, leading to a more compact design and reducing the required sample size.

## REFERENCES

- [1] Z. Feng, W. Liang, J. Ling, X. Xiao, K. K. Tan, and T. H. Lee, "Precision force tracking control of a surgical device interacting with a deformable membrane," *IEEE/ASME Trans. Mechatron.*, vol. 27, no. 6, pp. 5327–5338, Dec. 2022.
- [2] W. Liu, H. Ma, Z. Liu, Z. Xiong, and Y. Li, "Saturation-tolerant predefined space-time super twisting control and its application to piezoelectric fast steering mirror," *IEEE/ASME Trans. Mechatron.*, vol. 29, no. 2, pp. 1431–1440, Apr. 2024.
- [3] Z. Zhu et al., "A compliant self-stabilization nanopositioning device with modified active-passive hybrid vibration isolation strategy," *IEEE/ASME Trans. Mechatron.*, vol. 28, no. 6, pp. 3305–3316, Dec. 2023.
- [4] C. Dai et al., "Automated piezo-assisted sperm immobilization," *IEEE Trans. Autom. Sci. Eng.*, vol. 21, no. 3, pp. 2604–2612, Jul. 2024.
- [5] L. Gao, S. Yang, B. Meng, G. Tong, H. Fan, and G. Yang, "Frequency matching optimization model of ultrasonic scalpel transducer based on neural network and reinforcement learning," *Eng. Appl. Artif. Intell.*, vol. 117, 2023, Art. no. 105572.
- [6] M. Hofmann, A. Haeberlin, S. de Brot, A. Stahel, H. Keppner, and J. Burger, "Development and evaluation of a titanium-based planar ultrasonic scalpel for precision surgery," *Ultrasonics*, vol. 130, 2023, Art. no. 106927.
- [7] C. Dai et al., "Design and control of a piezo drill for robotic piezo-driven cell penetration," *IEEE Robot. Autom. Lett.*, vol. 5, no. 2, pp. 339–345, Apr. 2020.
- [8] G. Bernava et al., "Lithotripsy of calcified aortic valve leaflets by a novel ultrasound transcatheter-based device," *Front. Cardiovasc. Med.*, vol. 9, 2022, Art. no. 850393.
- [9] S. Permana, E. Grant, G. M. Walker, and J. A. Yoder, "A review of automated microinjection systems for single cells in the embryogenesis stage," *IEEE/ASME Trans. Mechatron.*, vol. 21, no. 5, pp. 2391–2404, Oct. 2016.
- [10] Y. Duan, J. Ling, Z. Feng, T. Ye, T. Sun, and Y. Zhu, "A survey of needle steering approaches in minimally invasive surgery," *Ann. Biomed. Eng.*, vol. 52, no. 6, pp. 1492–1517, 2024.
- [11] S. Zhang, Z. Chen, Y. Wu, and J. Zeng, "An ultrasonic orthopedic scalpel based on a sandwich piezoelectric transducer," in *Proc. 2021 IEEE Int. Ultrasonics Symp.*, 2021, pp. 1–4.
- [12] L. L. Howell, S. P. Magleby, and B. M. Olsen, *Handbook of Compliant Mechanisms*. Hoboken, NJ, USA: Wiley, 2013.
- [13] H. Huang, J. K. Mills, C. Lu, and D. Sun, "A universal piezo-driven ultrasonic cell microinjection system," *Biomed. Microdevices*, vol. 13, pp. 743–752, 2011.
- [14] P. Bilancia and G. Berselli, "An overview of procedures and tools for designing nonstandard beam-based compliant mechanisms," *Comput.-Aided Des.*, vol. 134, 2021, Art. no. 103001.
- [15] J. Ling, T. Ye, Z. Feng, Y. Zhu, Y. Li, and X. Xiao, "A survey on synthesis of compliant constant force/torque mechanisms," *Mechanism Mach. Theory*, vol. 176, 2022, Art. no. 104970.
- [16] T. Ye and Y. Li, "Synthesis of 2-DoF decoupled rotation stage with FeA-based neural network," *Processes*, vol. 11, no. 1, 2023, Art. no. 192.
- [17] W. Johnson et al., "A flexure-guided piezo drill for penetrating the zona pellucida of mammalian oocytes," *IEEE Trans. Biomed. Eng.*, vol. 65, no. 3, pp. 678–686, Mar. 2018.
- [18] X. Gao, H. Huang, L. Chen, S. Yan, Y. Li, and L. Sun, "Research on single cell precision cutting technology based on piezoelectric ultrasonic vibration," in *Proc. 2018 IEEE Int. Conf. Robot. Biomimetics*, 2018, pp. 21–26.
- [19] Y. Li, T. Ye, J. Ling, X. Xiao, and Z. Feng, "A novel F-shaped linear guiding mechanism based compliant positioning stage with restricted parasitic motion," *Precis. Eng.*, vol. 88, pp. 674–685, 2024.
- [20] W. Chen, X. Shi, W. Chen, and J. Zhang, "A two degree of freedom micro-gripper with grasping and rotating functions for optical fibers assembling," *Rev. Sci. Instrum.*, vol. 84, no. 11, 2013, Art. no. 115111.
- [21] X. Yuan, Y. Liu, H. Zou, J. Ji, T. Zhou, and W. Wang, "Design and analysis of a 2-D piezoelectric platform based on three-stage amplification and L-shaped guiding," *IEEE Trans. Instrum. Meas.*, vol. 71, Oct. 2022, Art. no. 7505712.
- [22] P. Bilancia and G. Berselli, "Design and testing of a monolithic compliant constant force mechanism," *Smart Mater. Structures*, vol. 29, no. 4, 2020, Art. no. 044001.
- [23] M. Jin, C. Ynchausti, and L. L. Howell, "Zero-curvature deformation properties and 3R pseudo-rigid-body model of large-deflection euler spiral beams," *Mechanism Mach. Theory*, vol. 183, 2023, Art. no. 105261.
- [24] B. Hargrove, A. Nastevska, M. Frecker, and J. Jovanova, "Pseudo rigid body model for a nonlinear folding compliant mechanism," *Mechanism Mach. Theory*, vol. 176, 2022, Art. no. 105017.
- [25] W. C. Young et al. *Roark's Formulas for Stress and Strain*. New York, NY, USA: McGraw-hill, 2002.
- [26] D. P. Kingma and J. Ba, "Adam: A method for stochastic optimization," in *Proc. 3rd Int. Conf. Learn. Representations*, San Diego, May 7–9, 2015, doi: 10.48550/arXiv.1412.6980.



**Tingting Ye** (Student Member, IEEE) received the B.S. and M.S. degrees in mechanical engineering from the School of Power and Mechanical Engineering, Wuhan University, Wuhan, China, in 2019 and 2022, respectively. She is currently working toward the Ph.D. degree in mechanical engineering with the Department of Industrial and Systems Engineering, The Hong Kong Polytechnic University, Hong Kong, China. Her research interests include micromanipulations and compliant mechanisms.



**Zhao Feng** (Member, IEEE) received the B.S. and Ph.D. degrees in mechanical engineering from the School of Power and Mechanical Engineering, Wuhan University, Wuhan, China, in 2014 and 2020, respectively.

From 2019 to 2020, he was also a Visiting Ph.D. Student with the Department of Electrical and Computer Engineering, National University of Singapore, Singapore. From 2020 to 2022, he was a Postdoctoral Fellow with the Faculty of Science and Technology, University of Macau, Macau, China. He is currently an Associate Professor with the School of Power and Mechanical Engineering, Wuhan University. His research interests include precision control, iterative learning control, nanopositioning, and robotics.



**Jie Ling** (Member, IEEE) received the B.S. and Ph.D. degrees in mechanical engineering from the School of Power and Mechanical Engineering, Wuhan University, Wuhan, China, in 2012 and 2018, respectively.

From August to November 2017, he was a Visiting Ph.D. Student with the Department of Automatic Control and Micro-Mechatronic Systems, FEMTO-st Institute, Besançon, France. From 2019 to 2020, he was a Postdoctoral Research Fellow with the Department of Biomedical Engineering, National University of Singapore, Singapore. Since 2020, he has been an Associate Professor with the College of Mechanical and Electrical Engineering, Nanjing University of Aeronautics and Astronautics, Nanjing, China. His research interests include mechanical design and precision motion control of piezoelectric nanopositioning systems and micromanipulation robots.



**Yangmin Li** (Senior Member, IEEE) received the B.S. and M.S. degrees in mechanical engineering from Jilin University, Changchun, China, in 1985 and 1988, respectively, and the Ph.D. degree in mechanical engineering from Tianjin University, Tianjin, China, in 1994.

He is currently a Full Professor with the Department of Industrial and Systems Engineering, The Hong Kong Polytechnic University, Hong Kong. His research interests include micro/nanomanipulation, compliant mechanism, precision engineering, robotics, multibody dynamics, and control.

Prof. Li is an Associate Editor of the *Mechatronics*, and the *International Journal of Control, Automation, and Systems*.